Check for updates

Boosting visible light photocatalytic oxidation of CO using Au nanocatalysts through synergistic preparation of an Fe-doped TiO_2 support and cold plasma treatment†

Tong Xu,[a] Bangyou Jia,[a] Kaiwei Yan,[a] Chenlong Wang,[a] Bin Zhu [ID] *[a] and Xiaosong Li*[b]

TiO_2-supported Au nanocatalysts are highly attractive for visible light photocatalysis owing to their efficient surface plasmon resonance (SPR) and superior intrinsic catalytic activity. The prevailing strategies to prepare high-performance plasmonic Au/TiO_2 include constructing highly active $Au–TiO_2$ interfaces by modulating the electronic and geometric properties of Au nanoparticles or the TiO_2 support. Herein, we report a synergism of an Fe-doped TiO_2 ($Fe@TiO_2$) support and cold plasma treatment for the preparation of an $Au/Fe@TiO_2$–P catalyst, enabling this Au nanocatalyst to outperform samples fabricated *via* classical methods for the visible light photocatalytic oxidation of CO. The key to this collaborative preparation is treating the Au species on $Fe@TiO_2$ derived from hydrothermal synthesis with cold plasma, which constructs large numbers of $Au–Fe@TiO_2$ interfaces by generating unique interactions between Au nanoparticles and the support. The $Au/Fe@TiO_2$–P catalyst features high dispersion of Au and abundant surface oxygen species, thus accelerating the visible light photocatalytic oxidation of CO along the hot-electron transfer reaction pathway. This investigation demonstrates a promising approach to design and construct high-performance supported Au nanocatalysts for visible light photocatalysis.

1 Introduction

Gold (Au) nanocatalysts show outstanding catalytic activity at low temperatures and have drawn increasing attention over the past 40 years.[1,2] Recently, it has been demonstrated that supported Au nanocatalysts are significantly promising plasmonic nanostructures to utilize solar energy in the fields of environment and energy owing to their efficient surface plasmon resonance (SPR) in the visible light region.[3,4] Supports usually have strong influences on the performance of plasmonic Au nanocatalysts.[5–7] Titanium dioxide (TiO_2), which possesses advantages of high stability, non-toxicity and low cost, has been extensively used to fabricate plasmonic Au nanocatalysts (Au/TiO_2) for catalyzing a variety of reactions under visible light irradiation.[8–12]

Previous studies have demonstrated that the performance of photocatalytic reactions highly depends on the features of

$Au–TiO_2$ interfaces.[13,14] For example, during visible light photocatalytic oxidation (PCO) of CO, Au nanoparticles and the TiO_2 support adsorb CO and O_2 molecules, respectively, but the rate-determining step of the reaction between activated CO and oxygen species occurs at the active sites of the $Au–TiO_2$ interface.[15,16] Therefore, great efforts have been undertaken to boost the activity of Au/TiO_2 catalysts by tailoring the properties of the interface. One of the most used strategies to construct highly active $Au–TiO_2$ interfaces is to modulate the structure and properties of the TiO_2 support. For example, the photocatalytic performance of Au/TiO_2 can be enhanced by creating oxygen vacancies (O_v) in the TiO_2 support owing to the favorable charge transfer at the $Au–TiO_2$ interface.[17] Jiang *et al.* reported that constructing O_v at the $Au–TiO_2$ interface enables a remarkable enhancement in the photocatalytic activity of the Au/TiO_2 nanotube catalyst, probably due to the favorable charge transfer at the interface.[18] In addition, Au nanoparticles and their interaction with the TiO_2 support contribute to the photocatalytic activity of Au/TiO_2 catalysts. Much stronger interaction between Au and TiO_2 leads to a smaller Au particle size, which benefits the formation of highly active sites for photocatalytic reactions.[19] Dou *et al.* reported that incorporation of Au nanoparticles onto TiO_2 nanofibers leads

[a] Laboratory of Plasma Catalysis, Dalian Maritime University, Dalian 116026, China. E-mail: binzhu@dlmu.edu.cn
[b] Laboratory of Plasma Physical Chemistry, School of Physics, Dalian University of Technology, Dalian 116024, China. E-mail: lixsong@dlut.edu.cn

† Electronic supplementary information (ESI) available. See DOI: https://doi.org/10.1039/d4cy01550a

2844 | *Catal. Sci. Technol.*, 2025, **15**, 2844–2851

This journal is © The Royal Society of Chemistry 2025

to efficient charge separation and O_2 activation by creating a highly active Au–TiO_2 interface that contributes to a significant enhancement in the photocatalytic oxidation of CO.[20] Apparently, the construction of highly active Au–TiO_2 interfaces for photocatalytic reactions is expected by cooperatively controlling Au nanoparticles and the TiO_2 support. However, this strategy is rarely reported due to the incompatibility of the low Tammann temperature (half of the bulk melting point in degrees Kelvin) of Au nanoparticles with the harsh conditions of TiO_2 fabrication.

The cold plasma technique provides a promising approach for constructing highly active Au–TiO_2 interfaces compared to classical methods. Cold plasma treatment performed at mild conditions benefits the dispersion and the formation of low-coordinated sites of Au nanoparticles by tuning the interaction between Au nanoparticles and support.[21–27] Furthermore, the high reactivity of cold plasma at low temperatures avoids undesired effects on the morphology of TiO_2 support when tailoring Au nanoparticles. Thus, the cold plasma technique enables the construction of highly active Au–TiO_2 interfaces via the collaborative modulation of Au nanoparticles and TiO_2 support.

Herein, we present a synergy of support and Au nanoparticles by treating the Au species on Fe-doped TiO_2 (Fe@TiO_2) derived from hydrothermal synthesis with O_2 plasma, which enables the Au/Fe@TiO_2 catalyst to outperform TiO_2-supported samples in the PCO of CO under visible light irradiation. We attribute the superior photocatalytic performance of Au/Fe@TiO_2 to the outstanding surface properties of Fe@TiO_2 to disperse Au nanoparticles and to the intimate interaction between Au nanoparticles and Fe@TiO_2 induced by O_2 plasma treatment to construct highly active sites at Au–Fe@TiO_2 interfaces. This investigation demonstrates that collaborative preparation of the TiO_2 support and cold plasma treatment can be exploited to design and construct high-performance plasmonic Au nanocatalysts.

2 Experimental

2.1 Construction of Au nanocatalysts

The plasma-treated Au/Fe@TiO_2 nanocatalyst was synthesized via two steps (Fig. 1). The first step was to synthesize the Fe@TiO_2 support using a hydrothermal synthesis method.[28,29] Briefly, 8.5 g of tetrabutyl titanate and 3 mL of glacial acetic acid were added into 15 mL of anhydrous ethanol, and the mixture was subjected to ultrasonic treatment until it became homogeneous. Subsequently, about 0.05 g of Fe(NO_3)$_3$·9H_2O was dissolved in 3 mL of deionized water and then mixed with the aforementioned mixture. After stirring for 10 minutes, the mixture was hydrothermally treated at 180 °C for 20 hours. The product obtained from hydrothermal synthesis was washed and dried overnight at 80 °C. Finally, the dried sample was calcined at 400 °C for 2 hours in air to obtain the Fe@TiO_2 sample. The TiO_2 sample was prepared by the same synthesis procedures without the addition of Fe precursor. Au was loaded onto Fe@TiO_2 via a modified impregnation method.[23] During the preparation, $HAuCl_4$ was used as the Au precursor and the impregnated samples were washed using ammonia water and deionized water to remove chlorine. After drying at 80 °C for 12 h, the fresh Au/Fe@TiO_2 sample was obtained. The Au loading was 0.91 wt% according to ICP-AES analysis (Shimadzu ICPE-9800, Japan).

The second step involved treating the fresh Au/Fe@TiO_2 nanocatalyst with O_2 plasma. Before O_2 plasma treatment, catalyst coatings of Au/Fe@TiO_2 nanocatalyst (30 ± 1 mg) were prepared on glass substrate (25 mm × 50 mm × 1 mm).[22] Plasma treatment of the catalyst coatings was performed in a home-made dielectric barrier discharge (DBD) reactor,[15] which consisted of two ceramic sheets (1 mm thickness) covered by silver coatings with a discharge gap of 1 mm. O_2 plasma was generated at an O_2 flow rate of 100 SCCM and an input power of 10 W, and the Au/Fe@TiO_2 nanocatalyst was treated for 10 min using a 2 kHz AC high-voltage source. The resulting catalyst was denoted as Au/Fe@TiO_2–P.

For comparison, the fresh Au/Fe@TiO_2 sample was treated by traditional calcination (in air at 200 °C for 2 h) during the second step to obtain the calcined sample of Au/Fe@TiO_2–C. Additionally, commercial TiO_2 (Degussa P25) and hydrothermally synthesized TiO_2 were used as the support to prepare two other catalyst counterparts: Au/P25 and Au/Fe@TiO_2, respectively. Au/P25 and Au/Fe@TiO_2 treated using O_2 plasma were denoted as Au/P25–P and Au/Fe@TiO_2–P, respectively.

2.2 Catalyst characterization

The crystalline structures of Au nanocatalysts were characterized by an X-ray diffractometer (X'Pert PRO, PANalytical, Nederland) equipped with Cu Kα radiation at a scanning speed of 5.0° min^{-1} with a scanning range (2θ) of 20–80°. The morphology of Au nanocatalysts were observed using a high-resolution transmission electron microscope (JEM-F200, JEOL Ltd, Japan) equipped with energy dispersive X-ray spectroscopy (EDS). The average size of Au nanoparticles was determined by measuring more than 200 individual nanoparticles. The surface chemical states of the samples were characterized by an X-ray photoelectron spectrometer (XPS, ESCALAB250, Thermo VG, USA)
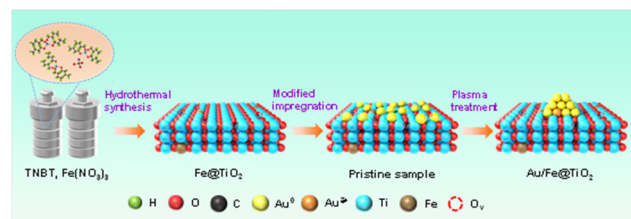

Fig. 1 Scheme showing the construction of the Au/Fe@TiO_2 nanocatalyst.

equipped with monochromatized Al Kα radiation, operated at 15 kV and 300 W. CO chemisorption measurements for the Au nanocatalysts were described in the Supporting Information. UV–vis diffuse reflectance spectra (UV–vis DRS) of the samples were measured using a lambda 750 s spectrometer (Perkin-Elmer, USA) within the wavelength range of 300–800 nm. Photoluminescence (PL) spectra were obtained using a spectrophotometer (F-7000, Hitachi, Japan) with an excitation wavelength of 300 nm. Photocurrent and electrochemical impedance spectroscopy (EIS) of the samples were measured via a three-electrode cell, which were described in the ESI.†

2.3 CO oxidation evaluation

The CO oxidation evaluations were performed in a continuous-flow flat-type reactor[25] using 300 SCCM of reactant gas containing 920 ppm CO and 20 vol% O_2 (N_2 balance) at atmospheric pressure and 25 °C. An LED lamp was applied to supply visible light (420–700 nm) for the photocatalytic reaction (the distance between the lamp and reactor was 1 cm), and the power density of the visible light irradiation was set to 58 mW cm^{-2}. A CO_x analyzer (GXH-3011 N, Huayun, China) was used to analyze the outlet gas online. CO conversion (X_{CO}) and the reaction rate of CO (r_{CO}) were defined using the following equations:

$$X_{CO} = \frac{C_{CO_2}^{out}}{C_{CO}^{out} + C_{CO_2}^{out}} \times 100\% \quad (1)$$

$$r_{CO} = \frac{F \cdot C_{CO}^{in} \cdot X_{CO}}{m_{Au}} \quad (2)$$

where $C_{CO_2}^{out}$ and C_{CO}^{out} represent the concentration of CO_2 and CO in the outlet gas, respectively, m_{Au} is the actual mass of Au in the catalyst, C_{CO}^{in} is the initial concentration of CO, and F is the total flow rate. During evaluating the reaction rate, CO conversion was controlled below 15% by changing the gas velocity.
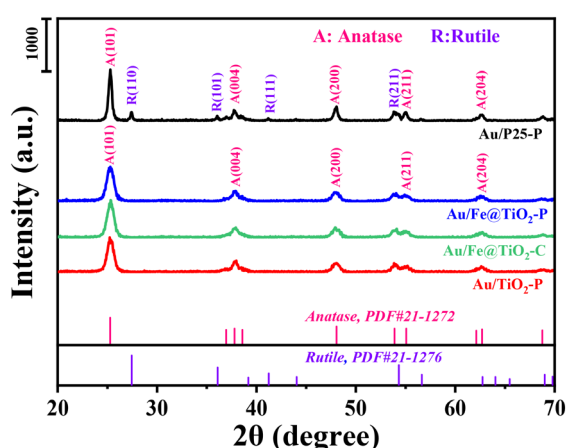

Fig. 2 XRD patterns of different TiO_2-supported Au nanocatalysts.

3 Results and discussion

3.1 Structure identification

Fig. 2 displays the XRD patterns of Au nanocatalysts supported on different TiO_2. For Au/P25–P, the rutile phase (PDF#21-1276) and anatase phase (PDF#21-1272) can be distinctly observed. In contrast, only the anatase phase is observed in Au/TiO_2–P, Au/Fe@TiO_2–P, and Au/Fe@TiO_2–C, which can be attributed to a relatively low synthesis temperature in the hydrothermal process.[30] TiO_2-supported Au nanocatalysts exhibit wider full-width at half-maximum (FWHM) of the (101) diffraction line than Au/P25–P (Fig. 2), indicating their much smaller primary particle size, with 12.6 nm for P25, 9.7 nm for TiO_2, and 8.9 nm for Fe@TiO_2, according to the Scherrer formula. Fe@TiO_2 consisting of smaller grains leads to an increase in the specific surface area (132 m² g^{-1}; Table S1†), which is larger than those of TiO_2 (103 m² g^{-1}) and P25 (49 m² g^{-1}). These data indicate that hydrothermal synthesis and appropriate Fe doping are necessary for synthesizing well-crystallized anatase phase TiO_2 with a high surface area. Fe doping shows no obvious influence on the diffraction patterns of Au nanocatalyst, due to the uniform doping of a small amount of Fe in TiO_2 during the synthesis. No Au reflections were found for either sample in the corresponding powder XRD patterns, indicating the presence of small Au entities at high dispersion.
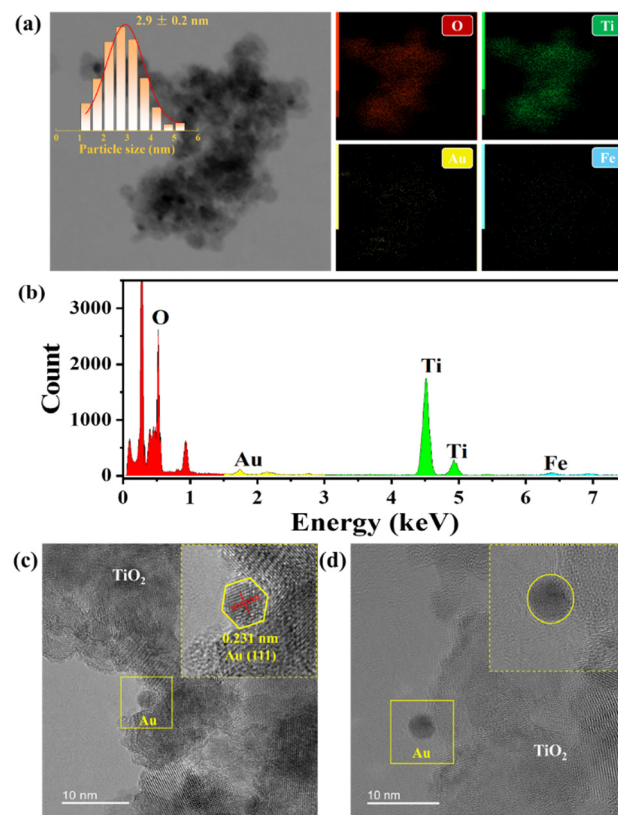

Fig. 3 (a) TEM image and corresponding Au nanoparticle size histograms of Au/Fe@TiO_2–P; EDS elemental mapping of O, Ti, Au and Fe; (b) EDS spectrum of Au/Fe@TiO_2–P; TEM images of Au nanoparticles of (c) Au/Fe@TiO_2–P and (d) Au/Fe@TiO_2–C.

Au nanoparticles on the TiO$_2$ support were observed by TEM. Au nanoparticles are uniformly dispersed on Fe@TiO$_2$ after O$_2$ plasma treatment (Fig. 3a). A very weak Fe signal is observed from the EDS mapping and spectrum (Fig. 3b), although 0.5 wt% Fe is doped into Fe@TiO$_2$ (the actual Fe doping amount of 0.42 wt% was determined by ICP-AES). This can be attributed to the low loading of Fe and its uniform distribution in Fe@TiO$_2$. The Au nanoparticles on Au/Fe@TiO$_2$–P can be clearly distinguished by identifying the lattice spacing of Au(111) from the high-resolution TEM (HRTEM) image (Fig. 3c). Furthermore, statistical results of the Au nanoparticle size indicate that the Au nanoparticles in Au/Fe@TiO$_2$–P show an average size of 2.9 nm (Fig. 3a), which is smaller than those of the calcined sample (3.7 nm; Fig. S1a†), Au/P25–P (3.6 nm; Fig. S1b†), and Au/TiO$_2$–P (3.3 nm; Fig. S1c†). The HRTEM image of the Au nanoparticle in Au/Fe@TiO$_2$–P presents clear corners and edges (Fig. 3c), and similar morphologies of the Au nanoparticles are also observed for Au/TiO$_2$–P and Au/P25–P (Fig. S2†). However, O$_2$ plasma treatment replaced by the calcination renders the Au nanoparticles relatively smooth for the calcined sample (Fig. 3d). The particle size and morphology features of Au nanoparticles in Au/Fe@TiO$_2$–P indicate that the plasma treatment enables the Au nanoparticles to obtain higher dispersion and coordination unsaturation. Considering that the unsaturated coordination sites at the interfaces between Au nanoparticles and the support play an important role for boosting the PCO reactions,[23,24] an outstanding performance can be expected of Au/Fe@TiO$_2$–P in visible light PCO of CO.

The electronic states of supported Au nanocatalysts were measured by XPS. Fig. 4 shows the spectra of Au 4f and O 1s, respectively, and the summarized results are listed in Table 1. Through the XPS spectra of Au 4f, the Au species in the plasma-treated samples can be deconvoluted into metallic Au (Au^0) and cationic Au species (Au$^{\delta+}$), where the Au$^{\delta+}$ species account for 81%, 70%, and 65% of the total Au in Au/P25–P, Au/TiO$_2$–P and Au/Fe@TiO$_2$–P, respectively. Besides a partial reduction of Au$^{\delta+}$ species during O$_2$ plasma treatment, the interaction between Au and the support also affects the content of Au$^{\delta+}$ in these samples. After an identical plasma treatment, Au/Fe@TiO$_2$–P exhibits the highest Au$^{\delta+}$ content, indicating that it has the strongest interaction of Au and Fe@TiO$_2$ compared to its counterparts, which is probably ascribed to the favorable formation of the oxygen vacancy (O$_v$) induced by Fe-doping.[31] The difference in interaction between Au and the support is also reflected by the shift of Au 4f$_{7/2}$ binding energy, and the Au^0 in Au/Fe@TiO$_2$–P obtains a positive shift of binding energy (+0.2 eV) compared to the other samples (Table 1), due to charge transfer towards Fe@TiO$_2$ induced by a strong interaction between Au and Fe@TiO$_2$. The content of Au$^{\delta+}$ highly depends on the treatment method. Only Au^0 is identified in Au/Fe@TiO$_2$–C (Fig. 4), indicating that the Au$^{\delta+}$ species are mostly reduced into Au^0 via calcination. The O 1s spectra of the Au nanocatalysts shown in Fig. 4 indicate that O can be deconvoluted into lattice oxygen (O$_l$) and surface oxygen
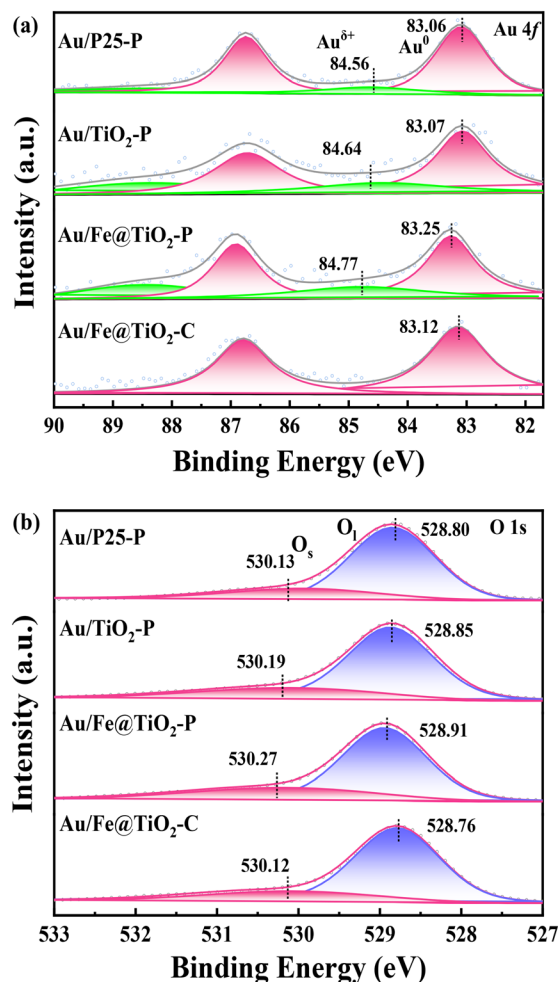

Fig. 4 XPS spectra of (a) Au 4f and (b) O 1s for Au nanocatalysts.

species (O$_s$),[32] where the content of O$_s$ is positively correlated to the Ti^{3+} content.[33] Large numbers of reactive species (*e.g.*, e, O$^-$, and O$_2^-$) in O$_2$ plasma facilitates the formation of Ti^{3+} (Fig. S3†), benefiting the formation of O$_v$. Thus, the O$_s$ content in different samples reflects the variation of O$_v$ concentrations. The content of O$_s$ for Au nanocatalysts obeys an order of Au/Fe@TiO$_2$–P (25 at%) > Au/TiO$_2$–P (22 at%) > Au/P25–P (20 at%) > Au/Fe@TiO$_2$–C (18 at%) (Table 1), indicating that Fe doping and O$_2$ plasma treatment favor the formation of O$_v$ in Au nanocatalysts. The Fe 2p spectra of Au/

Table 1 XPS analysis of Au nanocatalysts

Sample	Au 4f$_{7/2}$ (eV)		Au^0/Au (at%)	O$_s$/O (at%)
	Au^0	Au$^{\delta+}$		
Au/P25–P	83.1	84.6	81	20
Au/TiO$_2$–P	83.1	84.6	70	22
Au/Fe@TiO$_2$–P	83.3	84.8	65	25
Au/Fe@TiO$_2$–C	83.1	—	100	18

Note: Au = Au^0 + Au$^{\delta+}$, Au^0, and Au$^{\delta+}$ represent the metallic Au and cationic Au species, respectively; O = O$_s$ + O$_l$, O$_s$ and O$_l$ denote the surface and lattice oxygen, respectively.

This journal is © The Royal Society of Chemistry 2025

Catal. Sci. Technol., 2025, **15**, 2844–2851 | **2847**

Fe@TiO$_2$ samples show very weak signals (Fig. S4†) due to the low concentration of Fe on the surface of samples. These data suggest that the combination of Fe@TiO$_2$ synthesis and O$_2$ plasma treatment can effectively modulate the electronic properties and interaction between Au and the support in Au/Fe@TiO$_2$, which would play crucial roles in determining its photocatalytic activity and stability.

The accessibility and electronic properties of the supported Au nanocatalysts were studied by CO chemisorption DRIFTS. Au/P25–P shows CO adsorption signals at 2094 and 2164 cm^{-1}, due to the adsorption of CO molecules on metallic and cationic Au species,[23] respectively (Fig. 5). With the same exposure time of 30 min, an enhancement in the intensity of CO signals and blue-shift of the bands (from 2094 and 2164 cm^{-1} to 2096 and 2170 cm^{-1}, respectively) can be observed for Au/TiO$_2$–P. Au/Fe@TiO$_2$–P exhibits further enhancement in CO adsorption capacity and makes the CO adsorption band shift to 2099 cm^{-1}. The difference in CO adsorption capacity originates from the dispersion of Au in these samples: the smaller Au nanoparticles provide more unsaturated sites for CO adsorption,[23] while a blue-shift of the adsorption bands indicates an electron-deficiency of Au induced by enhanced interactions between Au and the support.[34] In contrast, traditional calcination results in Au/Fe@TiO$_2$–C displaying the weakest CO adsorption on metallic Au (2094 cm^{-1}) and cationic Au (2164 cm^{-1}), which is in good agreement with the TEM results. The CO chemisorption DRIFTS results demonstrate that the electronic properties of Au nanocatalysts highly depend on the support and treatment method, which is in good agreement with the XPS results.

3.2 Photoresponse characteristics

For the PCO of CO occurring over Au nanocatalysts under visible light irradiation, the driving force comes from the SPR
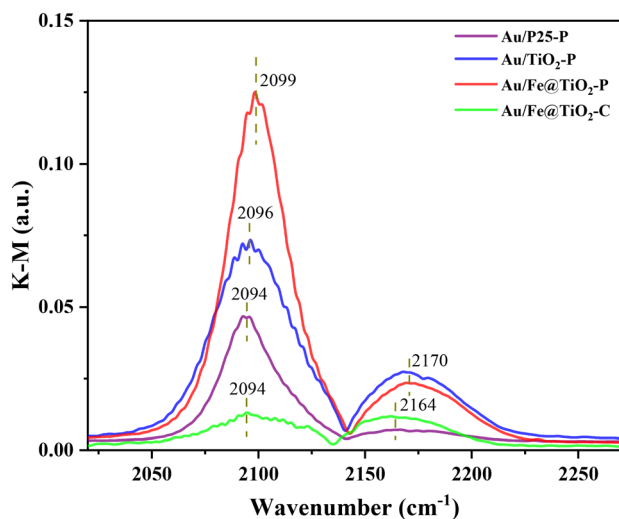

Fig. 5 *In situ* DRIFTS of CO adsorption on different Au nanocatalysts for an exposure time of 30 min.
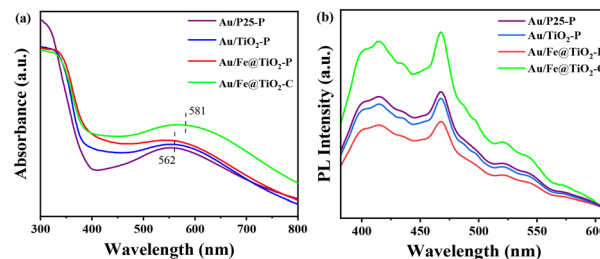

Fig. 6 (a) UV–vis DRS and (b) PL spectra of different Au nanocatalysts.

of Au nanoparticles.[35] Thus, we investigated the photoresponse characteristics of Au nanocatalysts using UV–vis DRS measurements. Au/P25–P, Au/TiO$_2$–P, and Au/Fe@TiO$_2$–P exhibit obvious absorption of visible light at around 562 nm due to the SPR effect of their metallic Au (Fig. 6a). Furthermore, the FWHM of absorption bands obey an order of Au/Fe@TiO$_2$–P > Au/TiO$_2$–P > Au/P25–P. Considering that the size of the plasmonic particle negatively correlates with the FWHM of the absorption band,[36,37] this order probably arises from the difference in Au nanoparticle size, consistent with the TEM results. The absorption band of Au/Fe@TiO$_2$–C also presents a red-shift (~19 nm) and enhanced intensity compared to plasma-treated samples, indicating a remarkable influence of the treatment method on the SPR effect of Au nanocatalysts. A strong light absorption band of Au/Fe@TiO$_2$–C is expected as almost complete reduction of Au$^{\delta+}$ into Au^0 was obtained in the calcination. The red-shift of the absorption band is attributed to an increased Au nanoparticle size and to the change in Au-support interactions caused by the different treatment methods. The transfer of hot-electrons generated *via* SPR to the support plays a crucial role in determining the photocatalytic activity of Au nanocatalysts,[38,39] which can be studied by measuring PL spectra of the samples. In general, intense PL peaks indicate a violent recombination and short lifetime of electron–hole pairs induced by visible light irradiation. The intensity of PL peaks for the plasma-treated samples is weakened compared to Au/Fe@TiO$_2$–C (Fig. 6b), suggesting that plasma treatment benefits the alleviation of the recombination of electron–hole pairs and prolongs the lifetime of charge carriers. Among the plasma-treated samples, Au/Fe@TiO$_2$–P exhibits the longest lifetime of photo-induced electrons, which is attributed to the suppressed recombination rate of electron–hole pairs on support caused by Fe doping.[40] These data suggest that the oxide supports determine the generation of driving force for the VLPCO of CO by controlling the reduction.

3.3 CO oxidation studies

To investigate the performance of supported Au nanocatalysts obtained by different preparation methods, CO oxidation reactions were performed over Au/P25–P, Au/TiO$_2$–P, Au/Fe@TiO$_2$–P, and Au/Fe@TiO$_2$–C. Visible light irradiation boosts CO conversion for each Au nanocatalyst due to the

2848 | *Catal. Sci. Technol.*, 2025, **15**, 2844–2851

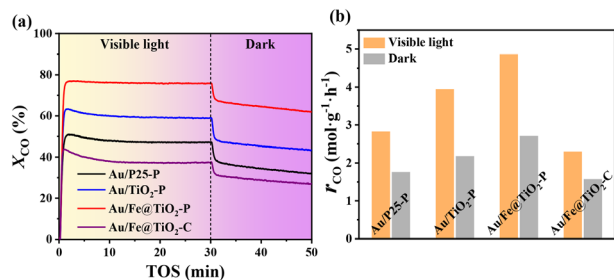This journal is © The Royal Society of Chemistry 2025

Fig. 7 Performance of different supported Au nanocatalysts in the CO oxidation reaction. (a) CO conversion as a function of TOS for different samples, and (b) the reaction rates of different samples with and without visible light irradiation.

Fig. 8 (a) Photocurrent density of different Au nanocatalysts under visible light irradiation, and (b) EIS Nyquist plots of the Au nanocatalysts.

SPR effect of Au nanoparticles (Fig. 7a). CO conversions over O_2 plasma-treated Au nanocatalysts follow the order of Au/Fe@TiO_2–P > Au/TiO_2–P > Au/P25–P with and without VL irradiation, indicating that hydrothermal-synthesized TiO_2 outperforms P25 in preparing Au nanocatalysts. Au/Fe@TiO_2–P exhibits better CO oxidation performance than Au/TiO_2–P owing to Fe-doped TiO_2 (Fig. 7a), but the performance of Au/Fe@TiO_2 highly depends on the treatment method. For example, calcination results in a poor performance of Au/Fe@TiO_2–C that is even worse than Au/P25–P. The doping amount of Fe affects the performance of Au nanocatalysts and Au/Fe@TiO_2–P with 0.5 wt% Fe obtaining the highest CO conversion (Fig. S5†), which is used for the comparison. Also, the conditions of plasma treatment (discharge power, atmosphere, and gas flow rate) strongly influence the performance of Au/Fe@TiO_2 in CO oxidation (Fig. S6†), and the highest performance is obtained by O_2 plasma treatment at 10 W and a flow rate of 100 SCCM. To accurately assess the response of Au nanocatalysts to visible light, we further measured the reaction rate of CO oxidation over different samples. Visible light irradiation enhances the amplitude of the reaction rate of different samples (Fig. 7b). Under the same visible light irradiation, the r_{CO} values of Au/Fe@TiO_2–C, Au/P25–P, and Au/TiO_2–P accelerate from 1.51-, 1.76-, and 2.23 mol g^{-1} h^{-1} to 2.32-, 2.81-, and 3.95 mol g^{-1} h^{-1}, respectively, and the largest enhancement of the reaction rate is obtained by Au/Fe@TiO_2–P from 2.71 to 4.89 mol g^{-1} h^{-1}. Furthermore, the stability of Au/Fe@TiO_2–P in CO oxidation was evaluated under visible light irradiation, and CO conversion (~77%) was quite stable during the 8 h continuous test (Fig. S7†), confirming a relatively good durability of active sites constructed by O_2 plasma. These data indicate that Fe-doped TiO_2 and O_2 plasma treatment are necessary for optimizing supported Au nanocatalysts (especially for plasmonic photocatalysis).

3.4 Electrochemical characterization

The hot-electron transfer behavior at the Au-support interface was investigated by photocurrent tests under visible light
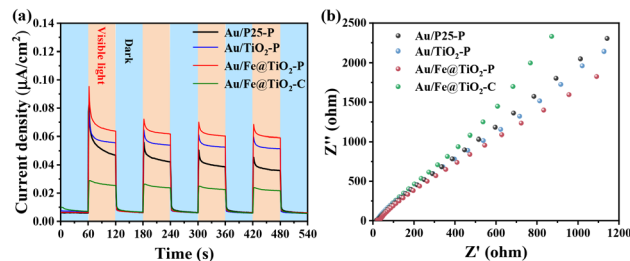
irradiation. All the Au nanocatalysts exhibit similar current densities in the dark (Fig. 8a). Visible light irradiation leads to a significant increase in current density due to the formation of hot-electrons. Favorable hot-electron transfer (corresponding to high current density) on the Au nanocatalysts suggests accelerated PCO of CO. The current density follows the order of Au/Fe@TiO_2–P > Au/TiO_2–P > Au/P25–P > Au/Fe@TiO_2–C (Fig. 8a), which is consistent with their photocatalytic activity (Fig. 7). Au/Fe@TiO_2–C shows much lower current density than the plasma-treated samples, although it possesses the strongest SPR effect under the same visible light irradiation (Fig. 6a). This demonstrates that the features of the Au-support interface play a decisive role in determining hot-electron transfer rather than the SPR effect. To further evaluate the efficiency of charge transfer at the Au-support interface, the Au nanocatalysts were analyzed using EIS Nyquist plots. The curves of Au/Fe@TiO_2–C present the largest radius among all samples, whereas the smallest radius of the curves is obtained by Au/Fe@TiO_2–P (Fig. 8b). This suggests that the treatment method has a significant influence on charge conduction resistance at the Au-support interface, since curve radius is directly related to the resistance at the catalyst interfaces and charge transfer efficiency.[21,41,42] In addition, Au/Fe@TiO_2–P exhibits lower charge transfer resistance than Au/TiO_2–P and Au/P25–P, indicating that the support of Fe@TiO_2 benefits the construction of the Au-support interface with low charge transfer resistance in O_2 plasma treatment. The photocurrent densities of different Au nanocatalysts are well explained by their charge conduction resistances deduced from EIS Nyquist plots, implying that the synergy of Fe@TiO_2 and O_2 plasma treatment can boost the PCO of CO over Au/Fe@TiO_2–P by accelerating the hot-electron transfer process at the constructed Au–Fe@TiO_2 interface.

3.5 Discussion

The mechanism of visible light PCO of CO is closely related to the features of Au-support interfaces of the Au nanocatalysts.[24,38,39] Herein, we propose that the PCO of CO follows the hot-electron transfer mechanism at the Au–Fe@TiO_2 interface, as described in Fig. 9. At this interface, O_2 adsorbs and combines with hot-electrons generated from the SPR of Au nanoparticles to form highly
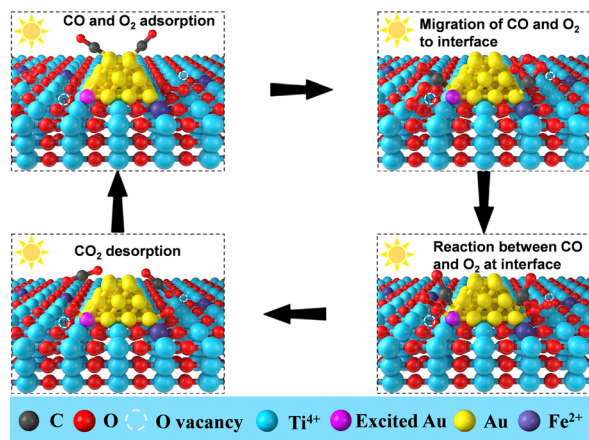
This journal is © The Royal Society of Chemistry 2025

Catal. Sci. Technol., 2025, **15**, 2844–2851 | **2849**

Fig. 9 Schematic of the proposed mechanism for visible light PCO of CO using the Au/Fe@TiO$_2$ nanocatalyst.

active O$_2^-$. The resulting O$_2^-$ further reacts with CO adsorbed on Au nanoparticles to form CO$_2$. The formation of O$_2^-$ species at the interface is a rate-determining step for the visible light PCO reactions.[43] Furthermore, the thermal oxidation process (in the dark) contributes to CO oxidation due to the adsorption and activation of O$_2$ at the Au–Fe@TiO$_2$ interface.

The synergistic enhancement of activity in PCO of CO for Au/Fe@TiO$_2$–P stems from the accelerated hot-electron transfer reaction pathway achieved by the combined preparation of Fe@TiO$_2$ support and O$_2$ plasma treatment. Compared to Au/P25–P and Au/TiO$_2$–P, Au/Fe@TiO$_2$–P exhibits better dispersion of Au nanoparticles (Fig. 3) and a larger number of unsaturated sites (Fig. 5) due to stronger interactions between Au and Fe@TiO$_2$. This results in the construction of more Au–Fe@TiO$_2$ interfacial active sites, thereby accelerating the rate of hot-electron transfer in the PCO of the CO reaction. Au/Fe@TiO$_2$–P with abundant O$_v$ induced by Fe-doping also exhibits higher O$_s$ content and low combination ability (Fig. 4 and Table 1), enabling efficient combination of surface oxygen species and hot-electrons from Au nanoparticles at the Au–Fe@TiO$_2$ interface, thus contributing to the increased PCO of CO In contrast, the low O$_s$ content and Au dispersion in Au/Fe@TiO$_2$–C restricts the construction of active Au–Fe@TiO$_2$ interfacial sites, limiting the CO oxidation reaction to proceed along the hot-electron transfer route under visible light irradiation.

4 Conclusions

We demonstrated a synergism of Fe@TiO$_2$ and Au nanoparticles for visible light PCO of CO based on a cooperative control of Fe@TiO$_2$ support synthesis and plasma treatment. The synergism on the PCO of CO is evidenced by the higher reaction rate (in the dark and under visible light irradiation) over Au/Fe@TiO$_2$–P compared with Au/Fe@TiO$_2$–C, Au/TiO$_2$–P, and Au/P25–P. The synergism renders Au/Fe@TiO$_2$–P the largest photo-induced

enhancement of the reaction rate from 2.71 to 4.89 mol g^{-1} h^{-1}. The catalyst characterizations indicate that Fe@TiO$_2$ prepared from hydrothermal synthesis exhibits high surface area and high-concentration of surface oxygen species, while O$_2$ plasma treatment controls the size of Au nanoparticles and leads to a strong interaction between Fe@TiO$_2$ and Au nanoparticles to modulate their electronic and geometric properties. The preparation of Au/Fe@TiO$_2$–P nanocatalyst through the synergistic combination of a Fe-doped TiO$_2$ support and cold plasma treatment features large numbers of Au–Fe@TiO$_2$ interfacial sites that is attributed to an accelerated hot-electron transfer pathway.

Data availability

The data supporting this article have been included as part of the ESI.†

Conflicts of interest

There are no conflicts to declare.

Acknowledgements

References

1 L. Li, S. Li, L.-F. Zhu, Y. Zheng and X.-B. Cao, *Catal. Sci. Technol.*, 2018, **8**, 1277–1287.

2 D.-W. Jeong, W.-J. Jang, J.-O. Shim, W.-B. Han, H.-S. Roh, U.-H. Jung and W.-L. Yoon, *Renewable Energy*, 2014, **65**, 102–107.

3 H.-Y. Lian, J.-L. Liu, X.-S. Li, X.-B. Zhu, A. Z. Weber and A.-M. Zhu, *Chem. Eng. J.*, 2019, **369**, 245–252.

4 Q. Fu, S. Kudriavtseva, H. Saltsburg and M. Flytzani-Stephanopoulos, *Chem. Eng. J.*, 2003, **93**, 41–53.

5 Y.-C. Li, X.-S. Li, B. Zhu, X.-B. Zhu, H.-Y. Lian and A.-M. Zhu, *J. Catal.*, 2022, **414**, 16–24.

6 H. Daly, A. Goguet, C. Hardacre, F. C. Meunier, R. Pilasombat and D. Thompsett, *J. Catal.*, 2010, **273**, 257–265.

7 H. H. Dong, Q. Z. Yang, Z. Y. Yang, Y. Y. Lan and W. L. Wang, *Appl. Surf. Sci.*, 2025, **684**, 161822.

8 J. H. Carter, P. M. Shah, E. Nowicka, S. J. Freakley, D. J. Morgan, S. Golunski and G. J. Hutchings, *Front. Chem.*, 2019, **7**, 443.

9 D. Andreeva, V. Idakiev, T. Tabakova and A. Andreev, *J. Catal.*, 1996, **158**, 354–355.

10 Y. Ming, L. F. Allard and M. F. Stephanopoulos, *J. Am. Chem. Soc.*, 2013, **135**, 3768–3771.

11 L. Q. Li, Y. P. Wang, Y. Ruan, T. F. Xu, S. Y. Wu and W. Y. Wu, *Appl. Surf. Sci.*, 2024, **672**, 160771.

12 W. Z. Zhang, Q. F. Li and H. A. Xia, *Appl. Surf. Sci.*, 2023, **613**, 156036.

2850 | *Catal. Sci. Technol.*, 2025, **15**, 2844–2851

This journal is © The Royal Society of Chemistry 2025

13 P. Pérez, M. A. Soria, S. A. C. Carabineiro, F. J. Maldonado-Hódar, A. Mendes and L. M. Madeira, *Int. J. Hydrogen Energy*, 2016, **41**, 4670–4681.

14 J. A. Rodriguez, *Catal. Today*, 2011, **160**, 3–10.

15 Y.-C. Li, X.-S. Li, B. Zhu and A.-M. Zhu, *Chem. Eng. J.*, 2022, **430**, 133013.

16 N. Liu, M. Xu, Y.-S. Yang, S.-M. Zhang, J. Zhang, W.-L. Wang, L.-R. Zheng, S. Hong and M. Wei, *ACS Catal.*, 2019, **9**, 2707–2717.

17 P. Yin, J. Yu, L. Wang, J. Zhang, Y. Jie, L. Chen, X. Zhao, H. Feng, Y. Yang, M. Xu, X. Zhang, J. Han, H. Yan and M. Wei, *J. Phys. Chem. C*, 2021, **125**, 20360–20372.

18 X. D. Jiang, C. Liu, Y. Zeng, G. X. Jiang, Y. Peng, S. Xu, Z. X. Wang and Z. M. Liu, *J. Phys. Chem. C*, 2025, **129**, 1485–1494.

19 W. D. Williams, M. Shekhar, W. S. Lee, V. Kispershy, W. N. Delgass, F. H. Ribeiro, S. M. Kim, E. A. Stach, J. T. Miller and L. F. Allard, *J. Am. Chem. Soc.*, 2010, **132**, 14018–14020.

20 T. W. Dou, Y. Y. Zhu, Z. Y. Chu, L. Sun, Z. J. Li and L. Q. Jing, *Appl. Catal., B*, 2024, **354**, 124112.

21 Z.-G. Sun, X.-S. Li, J.-L. Liu, Y.-C. Li, B. Zhu and A.-M. Zhu, *J. Catal.*, 2019, **375**, 380–388.

22 S. Zhang, X.-S. Li, B. Zhu, J.-L. Liu, X.-B. Zhu and A.-M. Zhu, *Catal. Today*, 2015, **256**, 142–147.

23 X.-Q. Deng, B. Zhu, X.-S. Li, J.-L. Liu, X.-B. Zhu and A.-M. Zhu, *Appl. Catal., B*, 2016, **188**, 48–55.

24 B. Zhu, L.-Y. Zhang, J.-L. Liu, X.-M. Zhang, X.-S. Li and A.-M. Zhu, *J. Hazard. Mater.*, 2021, **402**, 123508.

25 S. Zhang, W.-X. Zhao, A. Ren, B. Guo, Y. Dong and X.-Q. Deng, *Catal. Today*, 2019, **337**, 110–116.

26 J.-S. Zhang, L.-B. Di, F. Yu, D.-Z. Duan and X.-L. Zhang, *Nanomaterials*, 2018, **8**, 742.

27 X.-S. Li, X.-Y. Ma, J.-L. Liu, Z.-G. Sun, B. Zhu and A.-M. Zhu, *Catal. Today*, 2019, **337**, 132–138.

28 X. Wu, S. Yin, Q. Dong, C.-S. Guo, H.-H. Li, K. Takeshi and S. Tsugio, *Appl. Catal., B*, 2013, **142**, 450–457.

29 H.-P. Qi, Y.-Z. Liu, L. Chang and H.-L. Wang, *J. Environ. Chem. Eng.*, 2017, **5**(6), 6114–6121.

30 A.-H. Mamaghani, F. Haghighat and C.-S. Lee, *Chemosphere*, 2019, **219**, 804–825.

31 B. Santara, P.-K. Giri, S. Dhara, K. Imakita and M. Fujii, *J. Appl. Phys.*, 2014, **47**(23), 235304.

32 B. Zhu, Q.-W. Li, Y.-C. Li, Y.-Q. Xia, J.-L. Liu, A.-M. Zhou and X.-M. Zhang, *Chem. Eng. J.*, 2023, **469**, 143897.

33 W. Z. Zhang, X. X. Li, S. Y. Liu, J. H. Qiu, J. H. An, J. F. Yao, S. L. Zuo, B. Zhang, H. A. Xia and C. Z. Li, *ChemSusChem*, 2022, **15**, e202102158.

34 X. Liu, C.-Y. Mou, S. Lee, Y. Li, J. Secrest and B.-W.-L. Jang, *J. Catal.*, 2012, **285**(1), 152–159.

35 B. Zhu, C.-H. Zhong, B.-Y. Jia, T. Li, J.-L. Liu, Y.-C. Li and Y.-M. Zhu, *Chem. Eng. J.*, 2024, **480**, 148013.

36 P. Claus, A. Brückner, C. Mohr and H. Hofmeister, *J. Am. Chem. Soc.*, 2000, **122**, 11430–11439.

37 B. Zhu, X.-S. Li, J.-L. Liu, J.-B. Liu, X. Zhu and A.-M. Zhu, *Appl. Catal., B*, 2015, **179**, 69–77.

38 B. Zhu, X. Li, X.-Q. Deng, Y.-Q. Wang and L. L. Lu, *Plasma Chem. Plasma Process.*, 2022, **42**(3), 671–687.

39 B. Zhu, X. Li, Y. Li, J. Liu and X. Zhang, *Int. J. Mol. Sci.*, 2023, **24**(13), 10487.

40 M.-J. Valero-Romero, J.-G. Santaclara, L. Oar-Arteta, L. Van Koppen, D.-Y. Osadchii, J. Gascon and F. Kapteijn, *Chem. Eng. J.*, 2019, **360**, 75–88.

41 K. Yang, K. Huang, Z.-J. He, X. Chen, X.-Z. Fu and W.-X. Dai, *Appl. Catal., B*, 2014, **158**, 250–257.

42 T. V. Nguyen and O. B. Yang, *Catal. Today*, 2003, **87**, 69–75.

43 P. Christopher, H. Xin and S. Linic, *Nat. Chem.*, 2011, **3**(6), 467–472.

This journal is © The Royal Society of Chemistry 2025

Catal. Sci. Technol., 2025, **15**, 2844–2851 | **2851**